COAXIAL ELECTROSPINNING OF PROTEIN-ENCAPSULATED CORE-SHELL NANOFIBERS: PROCESS OPTIMIZATION AND RELEASE MODELING

by
Bhoomija Hariprasad

A Thesis
Submitted To
the Department of Biomedical Engineering,
University of Houston
in partial fulfillment of the requirements for the degree of

Master of Sciences

in Biomedical Engineering

Chair of Committee: Mohammad Reza Abidian, PhD

Committee Member: Chandra Mohan, PhD

Committee Member: Sheereen Majd, PhD

University of Houston
December 2019

DEDICATION

My thesis is dedicated to my wonderful family.

Firstly, I dedicate my thesis to my mother Harini, who has offered me unconditional love and support.

Secondly, to my father Hari, who constantly teaches me how to be strong, smart, and capable.

Lastly, to my little brother Krishna, who has been a source of joy and friendship for the last 15 years.

I aim to make you all proud every day.

ACKNOWLEDGMENTS

First and foremost, I would like to thank Dr. Mohammad Reza Abidian for the opportunity to grow as a researcher in his lab. I would like to thank my thesis committee members Dr. Chandra Mohan Majd and Dr. Sheereen Majd for their time and support. I would also like to thank Mohammadjavad Eslamian for his mentorship and guidance throughout this project. Finally, I would like to thank Nihir Patel for his assistance in nanofiber fabrication.

ABSTRACT

Coaxial electrospinning is a novel method for encapsulation of protein drugs into polymeric materials for use in drug delivery systems. In this study, coaxial electrospinning was used to fabricate aligned polyethylene oxide/poly(lactic-co-glycolic acid) core-shell nanofibers encapsulated with nerve growth factor (NGF), a trophic agent for axonal regeneration. Electrospinning processing parameters, namely inner and outer flow rates, wheel speed, needle-wheel distance, and applied voltage, were optimized using design of experiment (DOE) methodology to achieve nanofibers with minimized diameter and size distribution. The resulting prediction models were validated using analysis of variance. Optimized fibers were incubated in phosphate-buffered saline (PBS) for 3 days, and the released NGF was characterized at different time points using ELISA. The NGF release profile was mathematically modeled utilizing the Korsmeyer-Peppas and zero-order models. The results of this study can be applied to drug delivery systems for neural regeneration.

TABLE OF CONTENTS

LIST OF TABLES

LIST OF FIGURES

CHAPTER 1 : COAXIAL ELECTROSPINNING PROCESS OPTIMIZATION

1.1 Introduction

1.1.1 Coaxial Electrospinning

A large focus of tissue engineering concerns utilizing biomaterials and growth factors to induce repair and regeneration of organs and tissues. Nanostructures are particularly useful in axonal regeneration. Among the available techniques, electrospinning is a promising method to fabricate nanofibers formed by polymeric materials to be employed in tissue regeneration. Important characteristics of nanofibers include continuous and thin fibers, high surface-to-volume ratio, high porosity, and adjustable pore size distribution. Interconnected porous networks allow for cell attachment and nutrient transport [7].

Electrospinning is an especially effect technique for nanofiber fabrication because the methods are uncomplicated and the parameters are easy to control to achieve desired fiber sizes and dimensions [25]. The electrospinning apparatus consists of a syringe and syringe pump, high voltage power supply, a needle attached to the syringe, and a metal-based collector of the resulting fibers [7]. Once the electric field applied exceeds a critical value, the electrostatic force overcomes the melt, or the surface tension, of the polymer solution and cause a thin jet ejection of polymer from the needle tip onto the collector [12].

Many studies have been conducted in which single-component fibers have been generated via electrospinning, but a novel method termed coaxial electrospinning involves using two different polymer solutions to fabricate core-shell fibers [21].

Core-shell structures enhance the material properties of nanoscale materials [18]. The benefit of core-shell fibers lies in the improved controlled release of encapsulated biomolecules by adjusting fiber microstructure and fiber diameter [21].

Electrospinning is guided by system parameters, such as the viscosity, surface tension, and conductivity of the polymers used; as well as various process parameters including flow rates, applied voltage, distance between the needle and the disk collector, and the speed of the disk collector; these parameters should be optimized to achieve the appropriate fiber diameter and fiber alignment [25]. Additionally, diameter can be controlled by careful selection of solution concentrations, molecular weights, and solution conductivities [18].

Improved fiber alignment results in better contact guidance effects on neurite outgrowth [25]. For example, in a study by Wang et al., aligned poly(lactic-co-glycolic) acid nerve growth factor nerve guidance conduits (PLGA/NGF NFC) successfully combined physical guidance cues and biomolecular signals to mimic the extracellular matrix (ECM) [22]. Fiber morphology can be characterized using scanning electron microscopy (SEM) [23].

1.1.2 NGF Encapsulation

Neurotrophic factors guide the development, survival, and regeneration of neurons. They can be delivered via biomaterial-based scaffolds. A prominent example of a neurotrophic factor is nerve growth factor (NGF), which stimulates neurite outgrowth in sensory neurons and increases post-inflammation survival of sympathetic neurons [11]. NGF has been found to prevent retrograde degeneration of septal

cholinergic neurons [9]. Additionally, it was found that NGF binds to the endogenous collagen of rat sciatic nerves and maintains NGF activity both *in vivo* and *in vitro* [17]. Dontchev et al. investigated the effect of NGF on promoting reduction in growth cone collapse triggered by an alternate signaling molecule, Sema3A, in dorsal root ganglion (DRG) neurons [4]. Thus, NGF is extremely useful in the development of drug delivery systems.

Coaxial electrospinning is useful because growth factors can be encapsulated in the core-shell structure of the nanofibers. Several polymers have been explored for use in protein encapsulation. Yan et al used poly(l-lactide-co-ε-caprolactone)/bovine serum albumin-NGF (PLLACL/BSA-NGF) fibers to demonstrate sustained release of BSA from coaxially electrospun fibers [24]. In another study, Poly(Lactic Acid)/Silk Fibroin/Nerve Growth Factor (PS/N) fibers were coaxially electrospun, and through the use of PC12 cell culture it was determined that the encapsulated NGF exhibited sustained release, suggesting that the bioactivity of NGF was retained [19].

1.1.4 Design of Experiment Optimization

Response Surface Methodology (RSM) can be employed for optimizing controllable process parameters in nanofiber fabrication to achieve target sizes or dimensions [3]. RSM can provide closer confirmation of the response variable response to the desired response [2]. This method involves a statistical evaluation of the relationship between several independent variables in order to locate the optimal conditions to obtain the desired response value. After the appropriate design is implemented, the coefficients of the model are estimated using analysis of variance

(ANOVA), and the model is validated by comparing the predicted and experimental values [3].

The Box-Behnken Design (BBD) is a rotatable second-order design based on a three-level incomplete factorial design. Compared to other RSM designs, BBD has proven to be much more efficient than central composite design as well as three-level full factorial design. Additionally, BBD avoids combinations in which all parameters are simultaneously at their highest or lowest levels, as these regimes yield unsatisfactory results. Ultimately, BBD reduces the number of experimental runs required to obtain the optimum parameter conditions to achieve the desired response value [5]. Statistical analysis of the BBD can determine the interaction effect of the parameters on the response variables, and ANOVA can be used to determine if the prediction model obtained is valid [1]. Response surface plots can be used to visualize the function relationship between independent variables and response variables [13, 14, 15].

1.2 Methods

1.2.1 Materials

Poly(DL-lactide-co-glycolide) (50:50 DL-PLG, ester-terminated), with an inherent viscosity of 1.15 dL g^{-1}, was purchased from Lactel Absorbable Polymers. Benzyl triethylammonium chloride (BTEAC) and polyethylene oxide (PEO, M_w = 300,000) were obtained from Fisher Scientific. 10% BSA solution was obtained from R&D Systems. Chloroform (99.8%) was purchased from Acros-Organics. Fluorescein isothiocyanate conjugate bovine serum albumin (FITC–BSA) was purchased from Sigma Aldrich. A prebuilt coaxial needle (inner gauge number: 23, outer gauge

number: 18), polytetrafluoroethylene (PTFE) tubing kit and components for the coaxial needle were obtained from ramé-hart instrument co.

1.2.2 Coaxial Electrospinning

The setup for coaxial electrospinning is shown in Fig. 1.1.

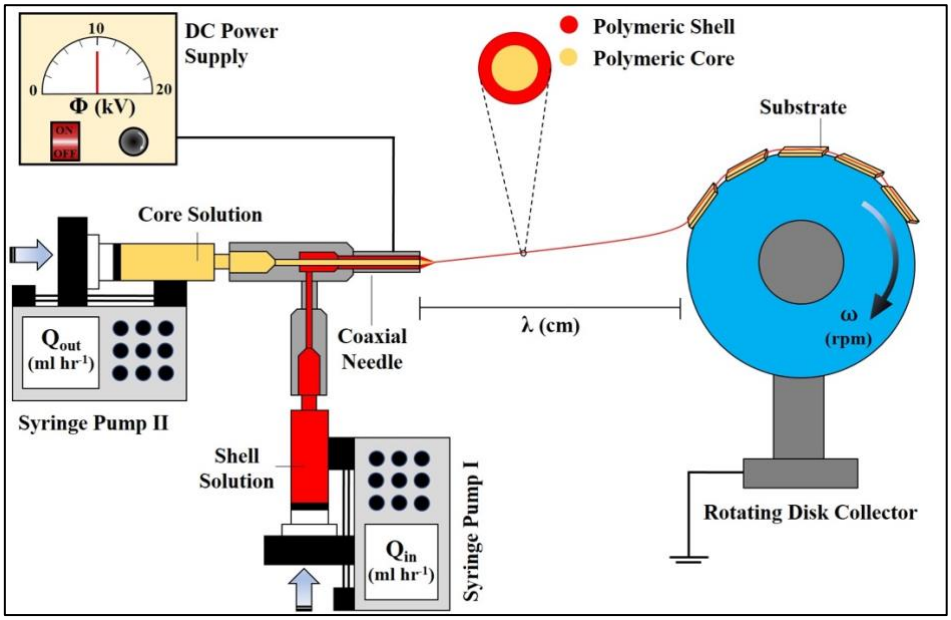

Figure 0.1: Coaxial Electrospinning Setup.

The polymeric shell solution was prepared by dissolving 661 mg PLGA (10 wt.%) in 4 ml of chloroform, an organic solvent. 13 mg of BTEAC was then added to the PLGA solution to increase the solution spinnability. NGF encapsulation was achieved in the polymeric core solution by adding 1 ml of NGF solution (22 µg NGF reconstituted with 1 ml of diluted BSA solution (0.22%)) into 3 ml of PEO solution (7 wt.%) consisting of 225 mg PEO in deionized water, thus forming an aqueous environment. To characterize NGF encapsulation, FITC-BSA was used as a model protein. In this case, the core solution was prepared by adding 1 ml of 1% (w/v) FITC-

BSA solution in deionized water into 3 ml of the PEO solution. To achieve homogenous core and shell solutions, each polymer mixture was stirred for an hour at room temperature (25℃). The stirred solutions were then delivered to the outer and inner coaxial needles using two programmable syringe pumps (obtained from Logato 100, KD Scientific) at various inner and outer flow rates (Q_{in} and Q_{out}). A high voltage power supply (PS/ER40P07, Glassman High Voltage, Inc.) was used to deliver high voltages (Φ) to the coaxial needle for coaxial electrospinning. The electrospun nanofibers were collected in aligned orientation on 1 cm × 0.5 cm plastic coverslips attached to the edge of a grounded rotating disk collector (disk diameter = 25 cm) controlled by a stepping motor (ω = disk speed) and located at a distance (λ) from the needle tip. The coaxial electrospinning was carried out at room temperature at a humidity of 30%.

1.2.3 Fiber Characterization

Samples prepared according to the BBD runs were imaged using a Field Emission Scanning Electron Microscope (FE-SEM, FEI 235). The diameter of the nanofibers visible in the collection of images for each sample was measured (n = 100) using ImageJ, a program provided by the National Institutes of Health. Additionally, fiber size distribution was calculated using the coefficient of variation (*C.V.*) as given by

$$\text{Fiber size distribution } (\%) = C.V. \times 100 = \left(\frac{\text{Standard error of mean}}{\text{Mean fiber diameter}}\right) \times 100. \quad (1\text{-}1)$$

To confirm protein encapsulation, the core-shell nanofibers underwent fluorescent imaging using the Zeiss AxioImager Z1 microscope.

1.2.4 Design of Experiment Optimization

The overall goal of optimization was to obtain a significantly low fiber diameter and distribution, defined as response variables. The controllable processing parameters, defined as factors included inner flow rate (Q_{in}), outer flow rate (Q_{out}), rotating collector speed (ω), applied voltage (Φ), and horizontal distance between the tip of the coaxial needle and the rotating disk (λ). The appropriate range of values for each factor was determined based on our prior experience with coaxial electrospinning (Q_{in} = 0.33 – 1 ml hr^{-1}, Q_{out} = 1 – 3 ml hr^{-1}, ω = 500 – 1000 rpm, Φ = 11 – 17 kV, and λ = 7 – 13 cm). DOE modeling was conducted using the JMP software developed by the SAS institute. The Box-Behnken design (BBD), based on a three-level incomplete factorial design, was chosen for its higher efficiency (calculated as the ratio of the number of model coefficients to the number of experimental runs) compared to typical response surface methods such as three-level full factorial design and central composite design (CCD) [5]. BBD is also advantageous because it excludes combinations at the extreme levels of all factors thus reducing the number of experimental runs and avoiding unsatisfactory results [5, 3].

The number of experimental runs generated in a BBD is calculated as

$$N = 2K\,(K-1) + C, \tag{1-2}$$

where N, K, and C are the number of runs, factors, and center-points, respectively [5]. In this study, K = 5 and C = 5, yielding a total number of 45 runs. Each factor in BBD is coded to reflect three levels; the lowest value in the range is coded as "–1", the center-point value is coded as "0", and the highest value in the range is coded as "+1" (Table 1.1).

Table 1.1: Coded Levels Of The Factors

Variable	Symbol	Coded Variable Level		
		Low (-1)	Center (0)	High (+1)
Inner Flow Rate (ml hr^{-1})	Q_{in}	0.33	0.665	1
Outer Flow Rate (ml hr^{-1})	Q_{out}	1	2	3
Rotating Disk Speed (rpm)	ω	500	750	1000
Applied Voltage (kV)	Φ	11	14	17
Needle-Disk Distance (cm)	λ	7	10	13

Prepared samples for each run in the BBD were imaged to allow determination of fiber diameter and distribution. Using these measured response values, the software generated a predictive model including prediction expressions for both response variables, surface plots illustrating the functional relationship between the factors and the response variables, and optimal parameter levels to obtain the target response values: minimized fiber diameter and fiber size distribution. A second-order polynomial equation was used to define the relationship between the variables and responses. The optimal parameter values were used to prepare an "optimized sample" to be used for NGF release assessment. The overall optimization process is depicted as a flowchart in Fig. 1.2 below.

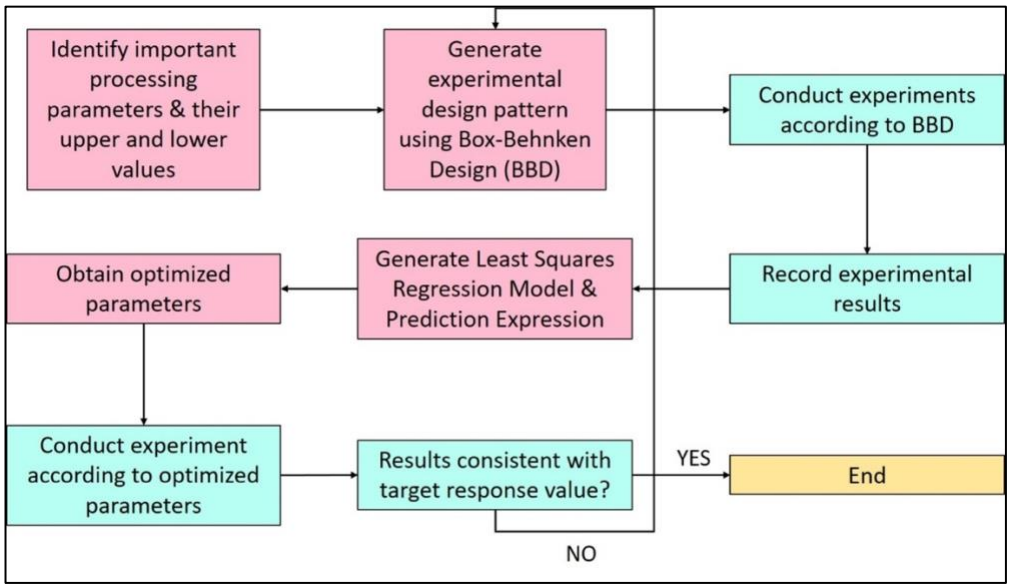

Figure 1.2: Box-Behnken Design Methodology.

1.3 Results & Discussion

1.3.1 Fiber Characterization

To characterize NGF encapsulation, FITC-BSA was used as a model protein. Fluorescent imaging confirmed protein encapsulation in the coaxial electrospun fibers as evidenced in Fig. 1.3 which displays the optimized fiber bundles.

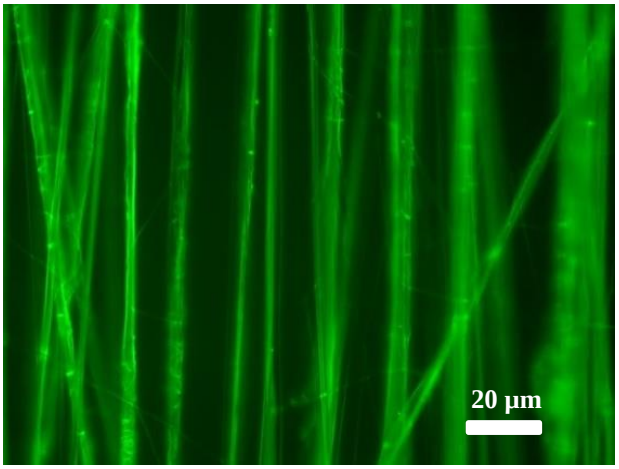

Figure 1.3: Fluorescent Imaging of Coaxial Electrospun Fibers to Confirm Protein Encapsulation

SEM imaging was done to visualize the coaxial electrospun fiber surface. The resulting image in Fig. 1.4 confirms fiber alignment and allow for visualization of fiber bundles.

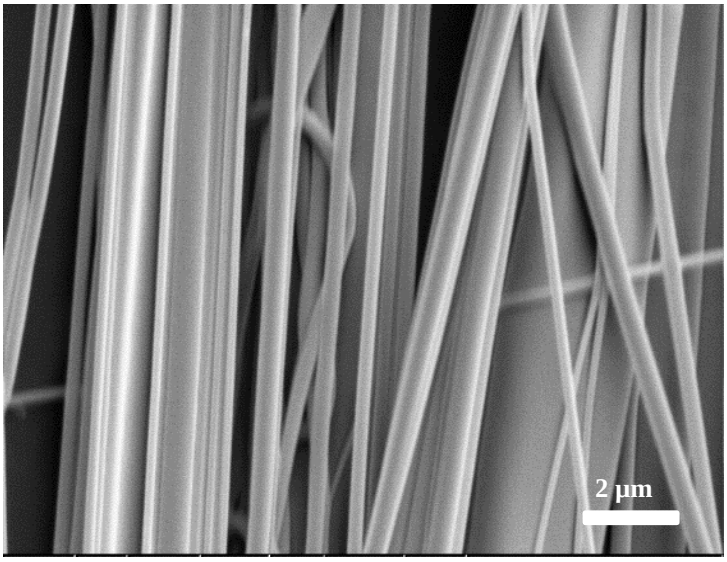

Figure 1.4: SEM Imaging to Confirm Nanofiber Alignment.

1.3.2 Design of Experiment Optimization

Inner flow rate (Q_{in}), outer flow rate (Q_{out}), collector speed (ω), applied voltage (Φ), and the needle-collector distance (λ) were identified as the controllable processing parameters for coaxial electrospinning of aligned core-shell nanofibers (Figure 1A). With a goal of minimizing fiber diameter and fiber size distribution of the electrospun nanofibers, the Box–Behnken design (BBD) was utilized to optimize the response variables. The experimental range of parameters used in the experiment the design were obtained from a previous single-parameter study (data not shown).

The BBD was comprised of 45 experimental runs with various combinations of parameter levels. The experimental results for the fiber diameter and fiber size distribution, determined by processing the SEM images using ImageJ, were used to construct predictive quadratic models given by

$$Y = \beta_0 + \beta_1\left(\frac{(Q_{in}-0.665)}{0.335}\right) + \beta_2(Q_{out}-2) + \beta_3\left(\frac{(\varpi-750)}{250}\right) + \beta_4\left(\frac{(\emptyset-14)}{3}\right) + \beta_5\left(\frac{(\lambda-10)}{3}\right) + \beta_{12}\left(\frac{(Q_{in}-0.665)}{0.335}\right)(Q_{out}-2) + \beta_{13}\left(\frac{(Q_{in}-0.665)}{0.335}\right)\left(\frac{(\varpi-750)}{250}\right) + \beta_{14}\left(\frac{(Q_{in}-0.665)}{0.335}\right)\left(\frac{(\emptyset-14)}{3}\right) + \beta_{15}\left(\frac{(Q_{in}-0.665)}{0.335}\right)\left(\frac{(\lambda-10)}{3}\right) + \beta_{23}(Q_{out}-2)\left(\frac{(\varpi-750)}{250}\right) + \beta_{24}(Q_{out}-2)\left(\frac{(\emptyset-14)}{3}\right) + \beta_{25}(Q_{out}-2)\left(\frac{(\lambda-10)}{3}\right) + \beta_{34}\left(\frac{(\varpi-750)}{250}\right)\left(\frac{(\emptyset-14)}{3}\right) + \beta_{35}\left(\frac{(\varpi-750)}{250}\right)\left(\frac{(\lambda-10)}{3}\right) + \beta_{45}\left(\frac{(\emptyset-14)}{3}\right)\left(\frac{(\lambda-10)}{3}\right) + \beta_{11}\left(\frac{(Q_{in}-0.665)}{0.335}\right)^2 + \beta_{22}(Q_{out}-2)^2 + \beta_{33}\left(\frac{(\varpi-750)}{250}\right)^2 + \beta_{44}\left(\frac{(\emptyset-14)}{3}\right)^2 + \beta_{55}\left(\frac{(\lambda-10)}{3}\right)^2, \quad (1\text{-}4)$$

where Y is the response value, β_0 is the model constant, and β_1- β_{55} are the regression coefficients calculated using experimental data. This equation uses the polynomial centering technique to adjust the parameter effects to achieve a higher accuracy of prediction. The constants and coefficients are presented in Table 1.2.

Table 1.2: The Coefficients for the Quadratic Models

Terms	Coefficient	Fiber Diameter (nm)				Fiber Size Distribution (%)			
		Estimate	S.E.	Lower 95%	Upper 95%	Estimate	S.E.	Lower 95%	Upper 95%
Constant	β_0	497.40	71.11	350.64	644.16	3.92	0.49	2.90	4.93
Q_{in}	β_1	88.92	39.75	6.88	170.96	0.31	0.28	-0.26	0.88
Q_{out}	β_2	29.01	39.75	-53.03	111.05	-0.38	0.28	-0.95	0.18
ω	β_3	66.53	39.75	-15.51	148.57	-0.03	0.28	-0.60	0.54
Φ	β_4	-276.05	39.75	-358.09	-194.01	-0.18	0.28	-0.74	0.39
λ	β_5	92.06	39.75	10.02	174.09	0.42	0.28	-0.15	0.99
$Q_{in} \times Q_{out}$	β_{12}	44.77	79.50	-119.31	208.85	0.23	0.55	-0.91	1.37
$Q_{in} \times \omega$	β_{13}	-40.38	79.50	-204.46	123.70	-0.27	0.55	-1.41	0.86
$Q_{in} \times \Phi$	β_{14}	-90.47	79.50	-254.55	73.61	0.49	0.55	-0.64	1.63
$Q_{in} \times \lambda$	β_{15}	-28.89	79.50	-192.97	135.19	-0.29	0.55	-1.43	0.85
$Q_{out} \times \omega$	β_{23}	-7.76	79.50	-171.84	156.31	-0.28	0.55	-1.42	0.86
$Q_{out} \times \Phi$	β_{24}	-63.60	79.50	-227.67	100.48	0.38	0.55	-0.76	1.52
$Q_{out} \times \lambda$	β_{25}	2.79	79.50	-161.29	166.86	-0.03	0.55	-1.17	1.11
$\omega \times \Phi$	β_{34}	62.75	79.50	-101.33	226.83	0.24	0.55	-0.90	1.37
$\omega \times \lambda$	β_{35}	53.54	79.50	-110.54	217.62	-0.23	0.55	-1.37	0.90
$\Phi \times \lambda$	β_{45}	-259.14	79.50	-423.21	-95.06	0.59	0.55	-0.55	1.72
Q_{in2}	β_{11}	-25.90	55.74	-140.95	89.15	-0.44	0.39	-1.23	0.36
Q_{out2}	β_{22}	81.76	55.74	-33.29	196.81	0.60	0.39	-0.20	1.40
ω_2	β_{33}	20.85	55.74	-94.20	135.90	0.90	0.39	0.10	1.69
Φ_2	β_{44}	197.41	55.74	82.36	312.46	-0.16	0.39	-0.95	0.64

Coefficients β_1- β_5 correspond to the linear terms, i.e. the effect of a single parameter on the response variable; β_{12}- β_{45} coefficients correspond to the interaction terms, indicating the effect of parameter interaction on the response variable; and β_{11}- β_{55} coefficients relate to the quadratic terms, or the effect of the interaction of a

parameter with itself. The responses at any regime in the interval of experimental design can be predicted by Eq. 1-4.

The experimental design as well as the experimental and predicted values of the response variables can be seen in Table 1.3.

Table 1.3: BBD Experimental Design with Comparison Between Actual and Predicted Values of the Fiber Diameter and Fiber Size Distribution

Run No.	Q_{in}	Q_{out}	ω	Φ	λ	Experimental Fiber Diameter[a] (nm)	Predicted Fiber Diameter (nm)	Experimental Fiber Size Dist. (%)	Predicted Fiber Size Dist. (%)
1	−1	0	−1	0	0	416	297	3.57	3.83
2	−1	−1	0	0	0	674	480	4.32	4.39
3	0	0	0	-1	+1	1566	1357	4.42	3.85
4	-1	0	0	0	+1	469	539	4.31	3.96
5	0	-1	0	0	+1	588	675	5.50	5.43
6	0	0	0	0	0	477	497	2.92	3.92
7	0	0	0	0	0	487	497	5.31	3.92
8	0	0	+1	+1	0	551	569	4.42	4.68
9	0	0	0	0	0	657	497	3.79	3.92
10	0	0	0	-1	-1	494	655	3.99	4.18
11	0	-1	0	-1	0	968	960	4.75	5.30
12	0	-1	+1	0	0	670	645	6.80	6.05
13	0	0	-1	0	+1	512	526	4.77	5.58
14	0	+1	0	0	-1	675	549	4.44	3.82
15	+	0	+	0	0	593	607	4.59	4.38
16	0	+1	0	0	+1	596	738	4.21	4.60
17	-1	0	+1	0	0	463	510	3.41	4.31
18	+1	0	0	0	+1	503	659	3.88	4.00
19	0	0	-1	+1	0	318	310	3.87	4.28
20	-1	+1	0	0	0	491	449	2.45	3.15
21	+1	0	0	-1	0	1114	1124	3.69	3.31
22	0	0	0	0	0	435	497	4.45	3.92
23	0	+1	0	-1	0	1358	1145	2.85	3.77
24	+1	0	-1	0	0	708	555	5.85	4.99
25	0	-1	-1	0	0	376	497	5.68	5.55
26	0	0	0	+1	-1	476	621	3.16	2.66
27	-1	0	0	-1	0	519	766	4.24	3.69
28	-1	0	0	0	-1	350	297	2.95	2.54
29	-1	0	0	+1	0	350	394	2.95	2.35
30	+	0	0	+	0	583	391	4.39	3.95
31	0	-1	0	0	-1	677	496	5.61	4.53
32	0	+1	-1	0	0	451	570	6.94	5.34
33	0	0	0	+1	+1	511	287	5.93	4.67
34	0	0	+1	0	+1	800	766	4.12	5.05
35	0	+1	+1	0	0	714	688	6.93	4.71
36	0	+1	0	+1	0	460	466	2.93	4.18
37	+	+	0	0	0	575	716	3.05	4.23
38	0	0	-1	-1	0	995	988	5.11	5.10
39	0	-1	0	+1	0	325	535	3.31	4.19
40	0	0	0	0	0	431	497	3.11	3.92
41	+1	0	0	0	-1	499	533	3.69	3.74
42	+1	-1	0	0	0	579	568	3.99	4.54
43	0	0	+1	-1	0	976	995	4.72	4.57
44	0	0	-1	0	-1	414	449	3.14	4.27
45	0	0	+1	0	-1	488	475	3.42	4.67
Optimum	-1	0	-1	+1	0	323	245	2.37	2.63

a) The fiber diameter for each run is the mean value of 100 measurements.

1.3.3 Parameter Effects

Eq. 1-4 displays the general prediction model for each response variable, fiber diameter and fiber size distribution. The linear, interaction, and quadratic effects of the process parameters, represented by the model coefficients, are presented in Table 1.2. The linear effects of Q_{in}, Q_{out}, ω, and λ were observed to have a positive correlation with fiber diameter, whereas Φ had a negative correlation on this response variable. Positive interaction coefficients signify a synergistic effect on the response value, while negative values indicate an antagonistic effect. The interactions $Q_{in} \times \omega$, $Q_{in} \times \Phi$, $Q_{in} \times \lambda$, $Q_{out} \times \omega$, $Q_{out} \times \Phi$, and $\Phi \times \lambda$ had an antagonistic effect. By contrast, the interactions $Q_{in} \times Q_{out}$, $Q_{out} \times \lambda$, $\omega \times \Phi$, and $\omega \times \lambda$ were found to have a synergistic effect. The quadratic effects of Q_{out}, ω, Φ, and λ were positive, while that of Q_{in} was negative.

The linear effects of Q_{in} and λ exhibited a positive correlation with fiber size distribution, whereas that of Q_{out}, ω, and Φ was negative for this response variable. The interactions $Q_{in} \times \omega$, $Q_{in} \times \lambda$, $Q_{out} \times \omega$, $Q_{out} \times \lambda$, and $\omega \times \lambda$ were antagonistic; conversely, the interactions $Q_{in} \times Q_{out}$, $Q_{in} \times \Phi$, $Q_{out} \times \Phi$, $\omega \times \Phi$, and $\Phi \times \lambda$ had a were synergistic. The quadratic effects of Q_{out}, ω, and λ were positive, while that of Q_{in} and Φ were negative.

Table 1.4 below presents the ANOVA results for the model. The p-values for Q_{in}, Φ, λ, $\Phi \times \lambda$, and Φ_2 indicated that they were significant model terms for fiber diameter, while ω_2 was a significant model term for fiber size distribution. The remainder of the model terms were not significant for either response variable.

Table 1.4: Analysis of Variance for Response Surface Quadratic Models

Terms	Fiber Diameter		Fiber Size Distribution	
	F ratio	P-value	F ratio	P-value
Quadratic model	4.6338	0.0003[a]	1.1018	0.4063
Q_{in}	5.0042	0.0348[a]	1.2509	0.2745
Q_{out}	0.5327	0.4725	1.9472	0.1757
ω	2.8017	0.1072	0.0132	0.9095
Φ	48.2282	<.0001[a]	0.4080	0.5290
λ	5.3633	0.0294[a]	2.3314	0.1399
$Q_{in} \times Q_{out}$	0.3171	0.5786	0.1764	0.6782
$Q_{in} \times \omega$	0.2580	0.6161	0.2490	0.6223
$Q_{out} \times \omega$	0.0095	0.9230	0.2617	0.6136
$Q_{in} \times \Phi$	1.2950	0.2664	0.8049	0.3785
$Q_{out} \times \Phi$	0.6399	0.4316	0.4805	0.4948
$\omega \times \Phi$	0.6230	0.4377	0.1823	0.6732
$Q_{in} \times \lambda$	0.1320	0.7195	0.2788	0.6023
$Q_{out} \times \lambda$	0.0012	0.9723	0.0029	0.9574
$\omega \times \lambda$	0.4536	0.5071	0.1786	0.6763
$\Phi \times \lambda$	10.6249	0.0033[a]	1.1284	0.2987
Q_{in2}	0.2158	0.6464	1.2750	0.2700
Q_{out2}	2.1514	0.1554	2.4027	0.1342
ω_2	0.1400	0.7116	5.3989	0.0289[a]
Φ_2	12.5416	0.0017[a]	0.1624	0.6906
λ_2	0.4026	0.5318	0.0441	0.8355
Lack of fit	3.3324	0.1256	1.2915	0.4452

a) Significant p-values.

To visualize the interaction effects of the processing parameters, three-dimensional (3D) response surface plots were generated based on the quadratic models for fiber diameter and fiber size distribution (Figure 1.5). Each 3D plot displays the functional relationship between two parameters and one response variable, while keeping the other parameters constant at their center-point values (given in Table 1.1).

The interaction of each pair of parameters can be explained by the contour profiles projected under the surface plots. The interaction response between Q_{in} and Q_{out} exhibits a parabolic cylinder for the fiber diameter (Fig. 1.5A) and a hyperbolic paraboloid for the fiber size distribution (Fig. 1.6A). As depicted by the accompanying

contour profiles, the minimum fiber diameter and fiber size distribution are obtained at low Q_{in} and medium Q_{out}.

The interaction response between Q_{in} and ω displays a nearly planar surface for the fiber diameter (Fig. 1.5B) but a hyperbolic paraboloid for the fiber size distribution (Fig. 1.6B). The minimum fiber diameter is achieved at low Q_{in} and low ω, while the minimum fiber size distribution occurs at low Q_{in} and medium ω. The interaction response between Q_{in} and Φ displays a nearly planar surface for the fiber diameter (Fig. 1.5C) and a paraboloid for the fiber size distribution (Fig. 1.6C). As depicted, the fiber diameter and fiber size distribution are minimized at low Q_{in} but high Φ values. The interaction response between Q_{in} and λ demonstrates a nearly planar surface for the fiber diameter (Fig. 1.5D) and a nearly parabolic cylinder for the fiber size distribution (Fig. 1.6D). Both fiber diameter and fiber size distribution are minimized at low Q_{in} and medium λ values. The interaction response between Q_{out} and ω displays a parabolic cylinder for the fiber diameter (Fig. 1.5E) and an elliptical cone for the fiber size distribution (Fig. 1.6E). As depicted, the minimum fiber diameter is achieved at medium Q_{out} and low ω, while the minimum fiber size distribution is obtained at medium Q_{out} and ω values. The interaction response between Q_{out} and Φ exhibits a nearly planar surface for the fiber diameter (Fig. 1.5F) and a hyperbolic paraboloid for the fiber size distribution (Fig. 1.6F). The minimum fiber diameter and fiber size distribution are achieved at medium Q_{out} and high Φ values. The interaction response between Q_{out} and λ demonstrates a parabolic cylinder for both fiber diameter (Fig. 1.5G) and fiber size distribution (Fig. 1.6G). As illustrated, both fiber diameter and fiber size distribution are minimized at medium Q_{out} and low λ values. The

interaction response between ω and Φ shows a nearly planar surface for the fiber diameter (Fig. 1.5H) and a parabolic cylinder for the fiber size distribution (Fig. 1.6H). The minimum fiber diameter is achieved at low ω and high Φ values, while the minimum fiber size distribution is obtained at medium ω and high Φ values. The interaction response between ω and λ exhibits a nearly planar surface for the fiber diameter (Fig. 1.5I) and a parabolic cylinder for the fiber size distribution (Fig. 1.6I). The minimum fiber diameter is achieved at low ω and λ values, while the minimum fiber size distribution is observed at medium ω and low λ values. The interaction response between Φ and λ for both fiber diameter (Fig. 1.5J) and fiber size distribution (Fig. 1.6J) demonstrate a non-planar shape with arbitrary contour profiles. According to these 3D plots, the fiber diameter is minimized at high Φ and λ values, while the minimum fiber size distribution is achieved at high Φ and low λ values.

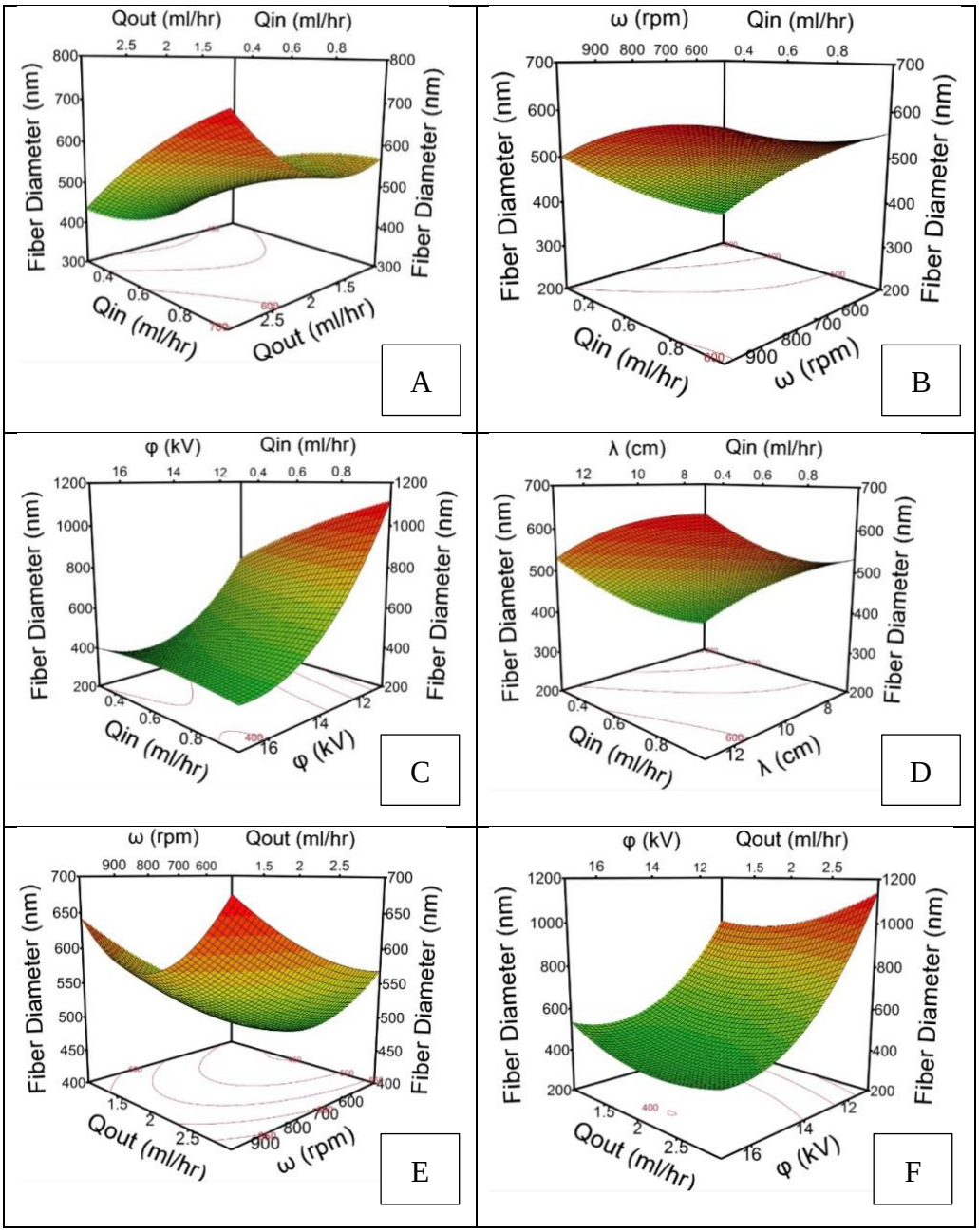
Qout (ml/hr)
Qin (ml/hr)
Fiber Diameter (nm)
A
ω (rpm)
Qin (ml/hr)
Fiber Diameter (nm)
B
φ (kV)
Qin (ml/hr)
Fiber Diameter (nm)
C
λ (cm)
Qin (ml/hr)
Fiber Diameter (nm)
D
ω (rpm)
Qout (ml/hr)
Fiber Diameter (nm)
E
φ (kV)
Qout (ml/hr)
Fiber Diameter (nm)
F

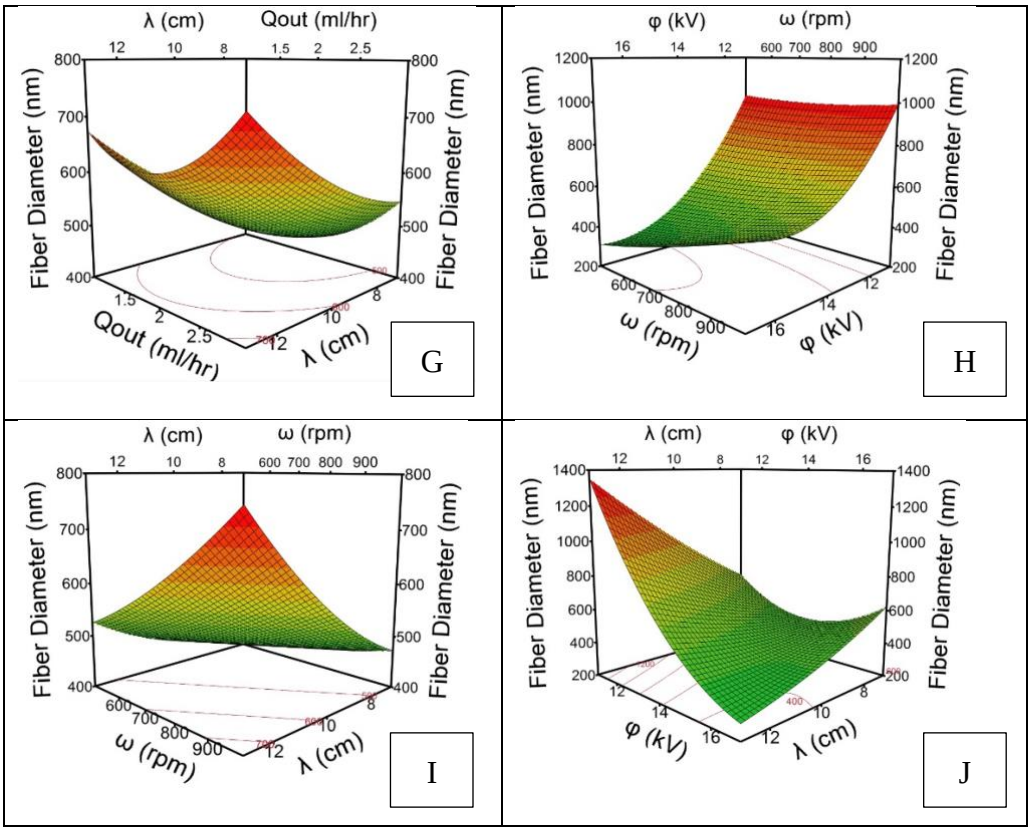

Figure 1.5: 3D Surface Plots for Fiber Diameter.

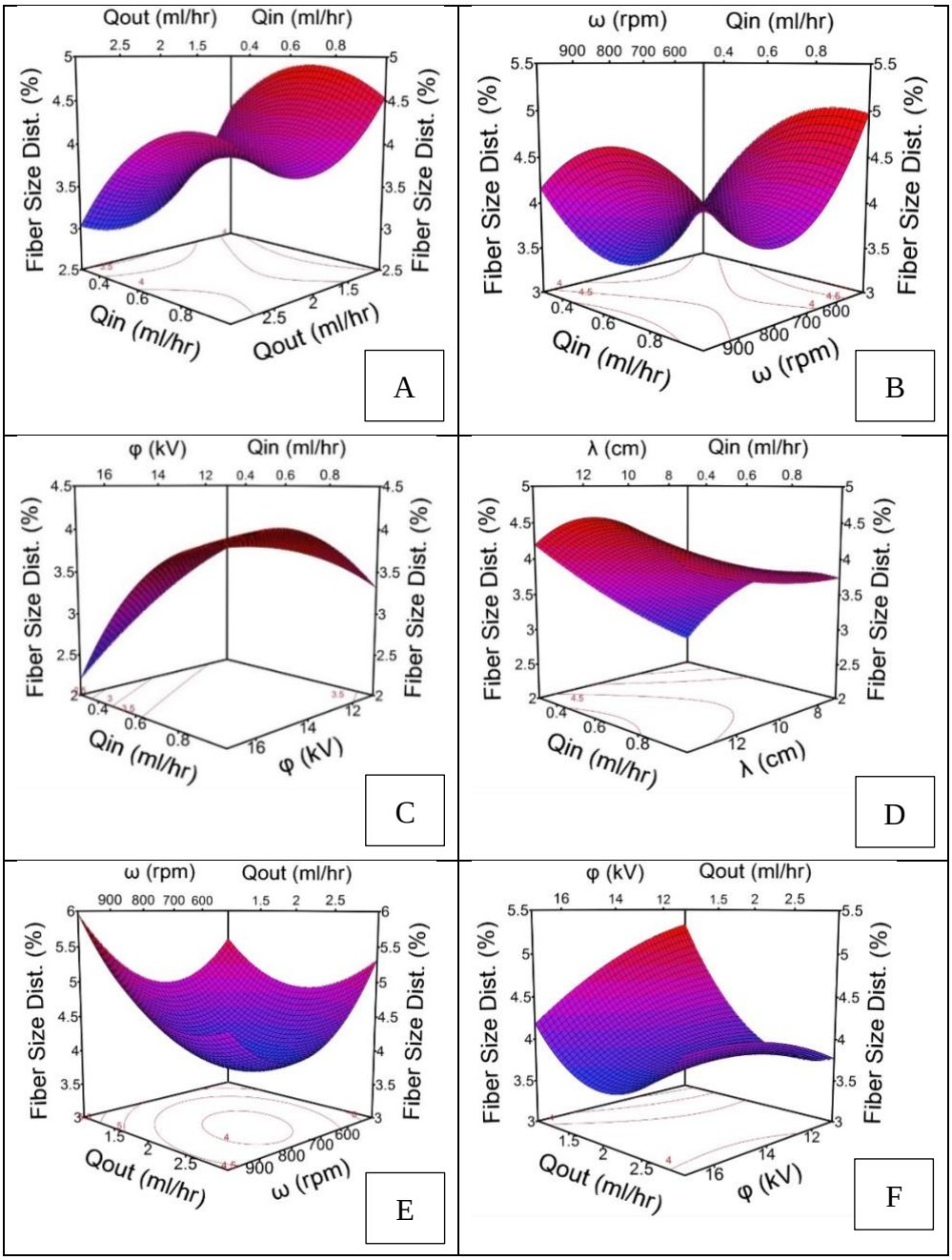
Qout (ml/hr)
Qin (ml/hr)
Fiber Size Dist. (%)
A
ω (rpm)
Qin (ml/hr)
Fiber Size Dist. (%)
B
φ (kV)
Qin (ml/hr)
Fiber Size Dist. (%)
C
λ (cm)
Qin (ml/hr)
Fiber Size Dist. (%)
D
ω (rpm)
Qout (ml/hr)
Fiber Size Dist. (%)
E
φ (kV)
Qout (ml/hr)
Fiber Size Dist. (%)
F

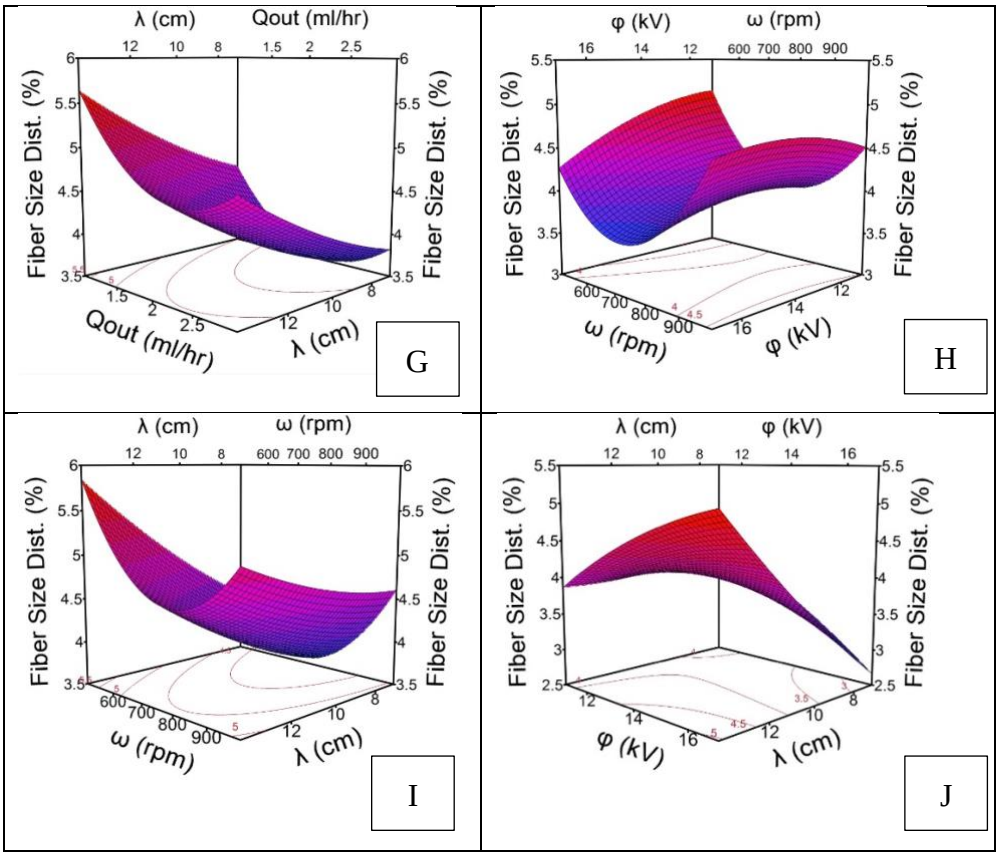

Figure 1.6: 3D Surface Plots for Fiber Size Distribution.

1.3.4 Model Validation

Diagnostic plots were generated to assess the adequacy of the regression model. The scatter plots of experimental versus predicted responses for fiber diameter and fiber size distribution alongside a "perfect fit line" (y=x) are displayed in Figure 1.5 and 1.6 below. As illustrated, the majority of the data points for the fiber diameter are arranged close to the perfect-fit line, while the data points for the fiber size distribution are comparatively more scattered around the perfect-fit line. R_2 was used as a measure of the degree to which the input variables explained the variation in the output variables. The R_2 for fiber diameter and fiber size distribution were 0.79 and

0.48, respectively, indicating that the quadratic model was an appropriate fit for fiber diameter, whereas it was not an adequate fit for fiber size distribution.

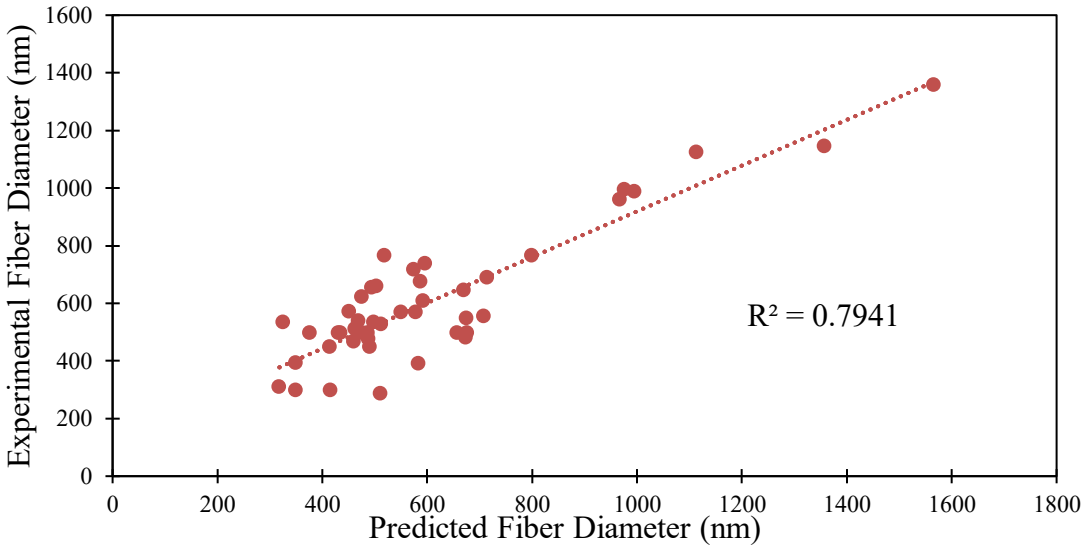

Figure 1.7: Experimental Versus Predicted Fiber Diameter.

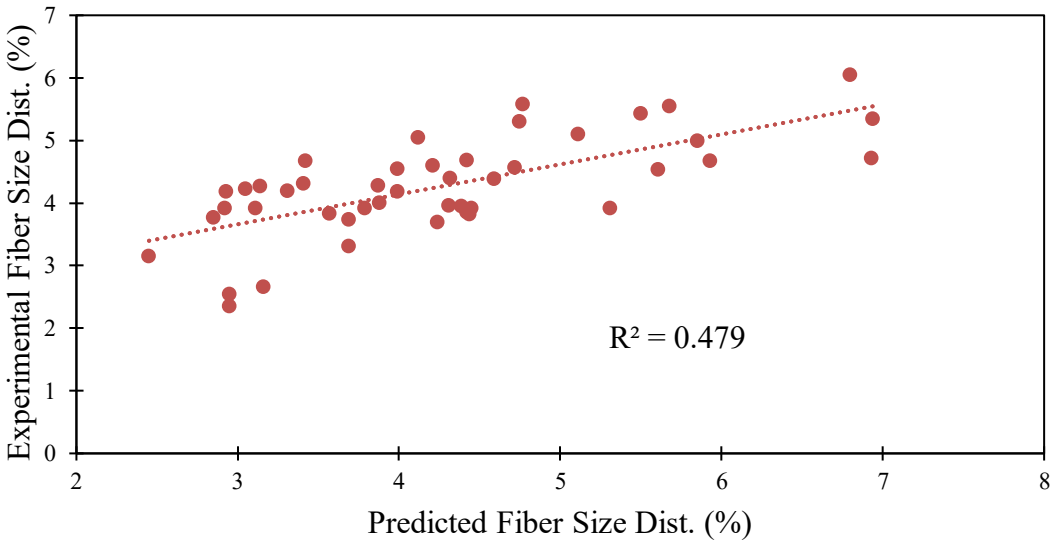

Figure 1.8: Experimental versus Predicted Fiber Size Distribution.

The studentized residual plots as a function of run number for the fiber diameter and fiber size distribution are presented in Figure 1.7 and 1.8 below. For both

response variables, the studentized residual plots represent a random scattering of data points, implying that the model prediction is valid. In general, studentized residuals must fall within the interval of -3.5 to +3.5, and experimental values should be disregarded for values beyond these limits [3]. Here, the studentized residuals for both fiber diameter and fiber size distribution were less than ±3.5, confirming the validity of the prediction.

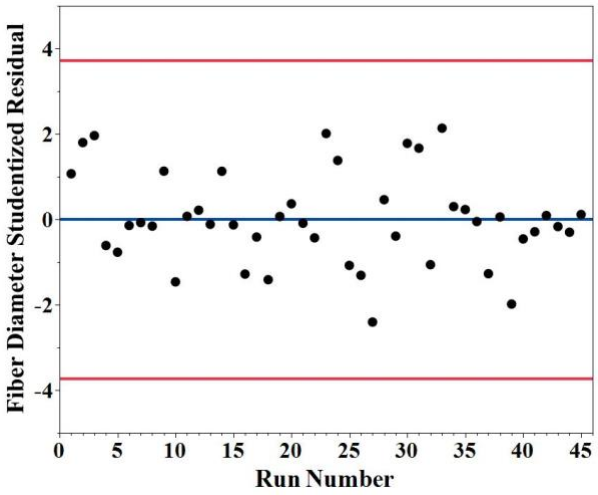

Figure 1.9: Studentized Residual for Fiber Diameter.

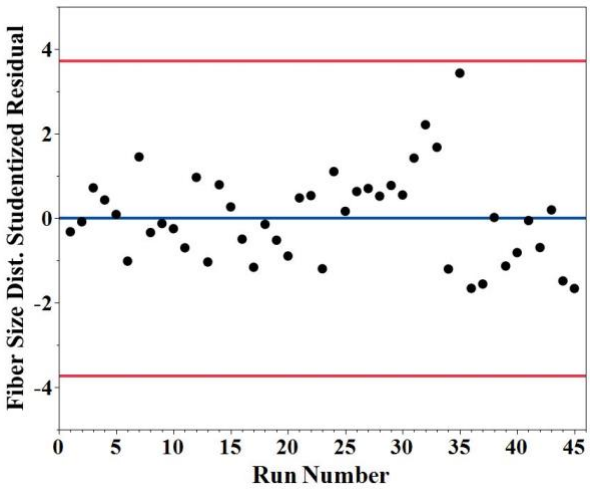

Figure 1.10: Studentized Residual for Fiber Size Distribution.

The model F-values for fiber diameter and fiber size distribution were 4.6338 and 1.1018, respectively, while the model p-values for fiber diameter and fiber size distribution were 0.0003 and 0.4063, respectively. These values indicate that the model was significant for fiber diameter but not for fiber size distribution. In addition, the "lack of fit" F values for fiber diameter and fiber size distribution were 3.3324 and 1.2915, respectively, while the corresponding p-values were 0.1256 and 0.4452, respectively, suggesting that the lack of fit was not significant for either response variable. These results can be seen in the ANOVA table (Table 1.4).

1.4 Conclusion

The goal of process optimization was to use the Box-Behnken Design to optimize the coaxial electrospinning parameters to obtained a minimized fiber diameter and fiber size distribution. The optimized parameters were used for coaxial electrospinning and minimal fiber diameter and size distribution were obtained. 3D surface plots were generated to visualize the functional relationship between the factors and the response

variables. Experimental versus predicted plots for each response variable visualized the accuracy of the model prediction. ANOVA confirmed that the resulting quadratic model was an appropriate fit for fiber diameter, but was not adequate for fiber size distribution. Potential future applications of this optimization method include optimizing additional properties of coaxially electrospun nanofibers, such as thickness of the shell polymer layer as well as the concentration of the encapsulated NGF. The results of this study can be applied towards future optimization of electrospun materials to achieve nanofibers of desired dimensional properties, paving the way for refinement of tissue engineering scaffolds for drug delivery.

CHAPTER 2 : NGF RELEASE MODELING

2.1 Introduction

The study of controlled release of biomolecules from polymeric systems is an important topic. Controlled drug release is useful in lowering the amount of drug required to achieve a therapeutic effect in patients, and can be optimized by controlling process parameters [18]. Of the different types of release, burst release is commonly observed in which an initial large bolus of the drug is released from the polymeric system before the release rate stabilizes. Burst release is unpredictable, making it difficult to control the release many drugs that need to be administered at varying rates for physiological recovery [6].

A current major challenge is developing a combination of mechanistic theories to describe the drug release from a polymeric system alongside mathematical models to similarly quantify drug transport in the human body [14].

Several mathematical models exist to quantify drug release from a delivery system. Normally, in diffusion-controlled systems, Fick's equations can adequately describe the drug dissolution process. An example of an empirical extension of Fick's law is the Korsmeyer-Peppas model, which describes the drug release kinetics at polymeric interfaces where conditions are not homogeneous throughout the entire diffusion process [8].

2.2 Methods

2.2.1 NGF Release Assessment

NGF encapsulated in the optimized core-shell nanofibers was detected using enzyme-linked immunosorbent assay (ELISA). Recombinant rat β-nerve growth factor (NGF), DuoSet ELISA kit for rat β-NGF, and 10% BSA solution were obtained from R&D Systems. Five samples were individually incubated in 1 ml of reagent diluent (1% BSA in PBS) at 37 °C for a total of 48 hrs. At predetermined time intervals (1 min, 5 min, 15 min, 30 min, 60 min, 90 min, 2 hr, 4 hr, 8 hr, 24 hr, and 48 hr), 250 ml of solution was extracted from each sample vial and replaced with an identical volume of fresh reagent diluent; these sample extracts were then assayed for NGF concentration. The ELISA assay was conducted in accordance with the protocol provided by the supplier, and each sample was analyzed in duplicate. A two-fold serial dilution of recombinant rat β-NGF standard was performed to generate a seven-point standard curve to identify the relationship between signal intensity (I) at 450 nm and the NGF concentration (C_{NGF}), given as

$$C_{NGF}\ (\mathrm{pg/ml}) = 243.9\ \mathrm{I} + 94.56. \quad (2\text{-}1)$$

SEM images were then taken of the fibers after NGF release to visualize the surface effects.

2.2.2 NGF Release Modeling

There are numerous mathematical models that have been developed to describe drug release from reservoir-based drug delivery systems. After fitting NGF release data to various kinetic models, the overall curve fitting was ultimately done via two

mathematical models. The first of these is the Korsmeyer-Peppas model. The corresponding equation is given by

$$\frac{M_t}{M_\infty} = Kt^n, \quad (2\text{-}2)$$

where $\frac{M_t}{M_\infty}$ is the fraction of drug released at time *t*, K is the release rate constant, and n is the release rate constant. This model is typically used to fit the first 60% of drug release from a polymeric system ($\frac{M_t}{M_\infty} < 0.6$) , which in this study corresponded to the burst release portion. The zero-order linear model was used to model the remainder of the release data, which corresponded to sustained NGF release.

2.3 Results & Discussion

2.3.1 NGF Cumulative Release

Eq. 2-1 was used to calculate the NGF concentration from the signal intensity at 450 nm. NGF concentration was plotted as a function of time as illustrated below. The release data exhibits a period of burst release followed by sustained release as seen below.

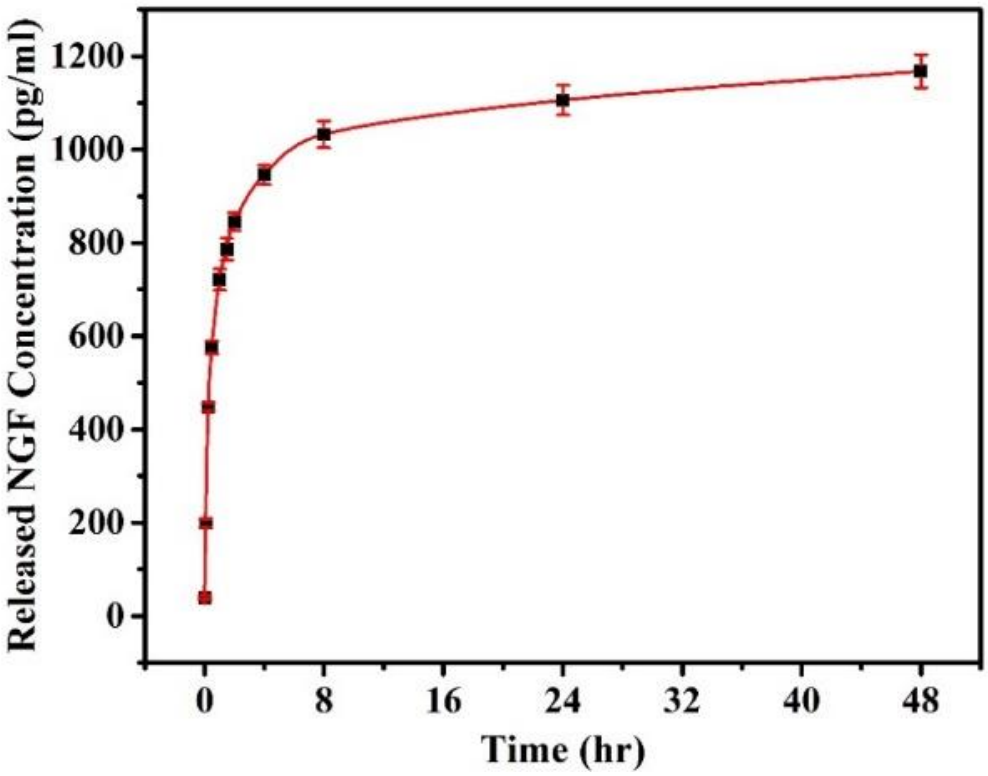

Figure 2.1: Cumulative NGF Release from Coaxial Electrospun Fibers.

Following NGF release, SEM images were taken again to demonstrate the resulting degradation of the fibers. The images indicate that the nanofibers fuse following NGF release, leading to clumps that can be visualized in Fig. 2.2 below.

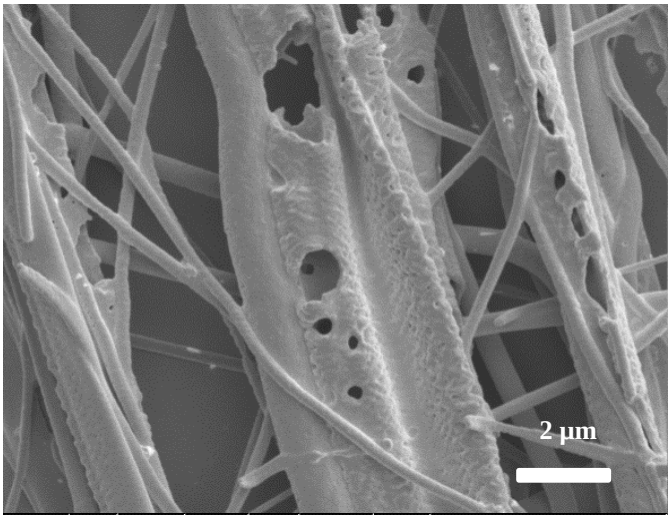

Figure 2.2: SEM Image Of Nanofibers Following NGF Release.

2.3.2 NGF Release Modeling

The Korsmeyer-Peppas model was used to model the first 60% of the release data, corresponding to the burst release of NGF. The obtained n-value for the Korsmeyer-Peppas model was 0.44, suggesting a non-Fickian diffusion mechanism [10].

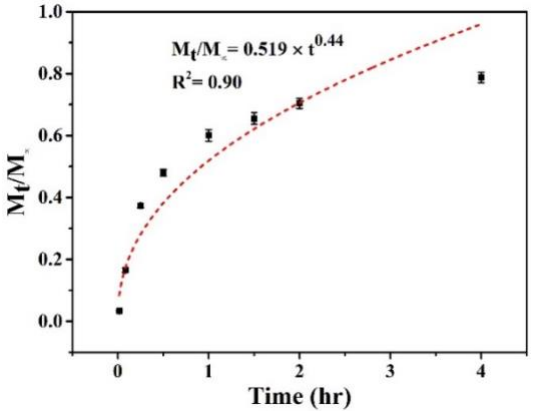

Figure 2.3: Korsmeyer-Peppas Model for Burst Release.

The remainder of the release data exhibited sustained release of NGF, which followed the zero-order kinetics model, evidenced by the high correlation coefficient provided in the figure below.

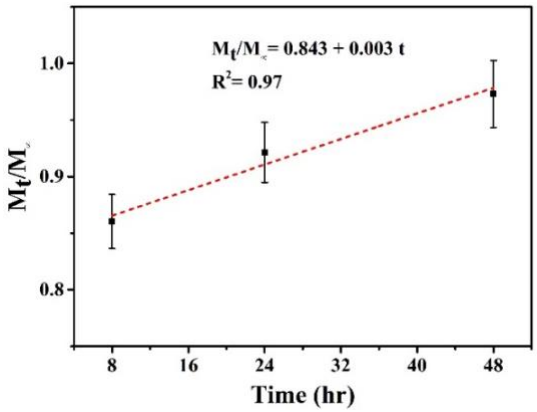

Figure 2.4: Zero-Order Linear Model for Sustained Release.

2.4 Conclusion

The goal of this study was to obtain cumulative NGF release data versus time from the optimized coaxial electrospun fibers, then mathematically model this release. The Korsmeyer-Peppas model was used to represent the initial burst release portion of the graph, covering approximately 60% of the data. The remaining sustained release data was modeled by the zero-order linear model. The high correlation coefficients confirmed the adequacy of each model which when put together encompassed all of the data points for NGF release. The results of this study can be applied to characterizing burst and sustained release from diffusion-controlled drug delivery systems fabricated using polymeric materials.

REFERENCES

1. Abul Kalam, M., Khan, A. A., Khan, S., Almalik, A., & Alshamsan, A. (2016). Optimizing indomethacin-loaded chitosan nanoparticle size, encapsulation, and release using Box–Behnken experimental design. *International Journal of Biological Macromolecules*, *87*, 329–340. https://doi.org/10.1016/j.ijbiomac.2016.02.033
2. Ahmad, A. L., Ismail, S., & Bhatia, S. (2005). Optimization of Coagulation−Flocculation Process for Palm Oil Mill Effluent Using Response Surface Methodology. *Environmental Science & Technology*, *39*(8), 2828–2834. https://doi.org/10.1021/es0498080
3. Ba-Abbad, M. M., Chai, P. V., Takriff, M. S., Benamor, A., & Mohammad, A. W. (2015). Optimization of nickel oxide nanoparticle synthesis through the sol–gel method using Box–Behnken design. *Materials & Design*, *86*, 948–956. https://doi.org/10.1016/j.matdes.2015.07.176
4. Dontchev, V. D., & Letourneau, P. C. (2003). Growth cones integrate signaling from multiple guidance cues. *The Journal of Histochemistry and Cytochemistry: Official Journal of the Histochemistry Society*, *51*(4), 435–444. https://doi.org/10.1177/002215540305100405
5. Ferreira, S. L. C., Bruns, R. E., Ferreira, H. S., Matos, G. D., David, J. M., Brandão, G. C., dos Santos, W. N. L. (2007). Box-Behnken design: An alternative for the optimization of analytical methods. *Analytica Chimica Acta*, *597*(2), 179–186. https://doi.org/10.1016/j.aca.2007.07.011

6. Huang, X., & Brazel, C. S. (2001). On the importance and mechanisms of burst release in matrix-controlled drug delivery systems. *Journal of Controlled Release*, *73*(2–3), 121–136. https://doi.org/10.1016/S0168-3659(01)00248-6
7. Ji, W., Yang, F., van den Beucken, J. J. J. P., Bian, Z., Fan, M., Chen, Z., & Jansen, J. A. (2010). Fibrous scaffolds loaded with protein prepared by blend or coaxial electrospinning. *Acta Biomaterialia*, *6*(11), 4199–4207. https://doi.org/10.1016/j.actbio.2010.05.025
8. Jou, D., Camacho, J., & Grmela, M. (1991). On the nonequilibrium thermodynamics of non-Fickian diffusion. *Macromolecules*, *24*(12), 3597–3602. https://doi.org/10.1021/ma00012a021
9. Kromer, L. F., & Cornbrooks, C. J. (1987). Identification of trophic factors and transplanted cellular environments that promote CNS axonal regeneration. *Annals of the New York Academy of Sciences*, *495*, 207–224. https://doi.org/10.1111/j.1749-6632.1987.tb23676.x
10. Mircioiu, C., Voicu, V., Anuta, V., Tudose, A., Celia, C., Paolino, D., … Mircioiu, I. (2019). Mathematical Modeling of Release Kinetics from Supramolecular Drug Delivery Systems. *Pharmaceutics*, *11*(3), 140. https://doi.org/10.3390/pharmaceutics11030140
11. Mohtaram, N. K., Montgomery, A., & Willerth, S. M. (2013). Biomaterial-based drug delivery systems for the controlled release of neurotrophic factors. *Biomedical Materials*, *8*(2), 022001. https://doi.org/10.1088/1748-6041/8/2/022001

12. Pan, H., Li, L., Hu, L., & Cui, X. (2006). Continuous aligned polymer fibers produced by a modified electrospinning method. *Polymer*, *47*(14), 4901–4904. https://doi.org/10.1016/j.polymer.2006.05.012
13. Ravanfar, R., Tamaddon, A. M., Niakousari, M., & Moein, M. R. (2016). Preservation of anthocyanins in solid lipid nanoparticles: Optimization of a microemulsion dilution method using the Placket–Burman and Box–Behnken designs. *Food Chemistry*, *199*, 573–580. https://doi.org/10.1016/j.foodchem.2015.12.061
14. Salazar, J., Heinzerling, O., Müller, R. H., & Möschwitzer, J. P. (2011). Process optimization of a novel production method for nanosuspensions using design of experiments (DoE). *International Journal of Pharmaceutics*, *420*(2), 395–403. https://doi.org/10.1016/j.ijpharm.2011.09.003
15. Shakeel, F., Haq, N., Alanazi, F. K., & Alsarra, I. A. (2014). Box–Behnken Statistical Design for Removal of Methylene Blue from Aqueous Solution Using Sodium Dodecyl Sulfate Self-microemulsifying Systems. *Industrial & Engineering Chemistry Research*, *53*(3), 1179–1188. https://doi.org/10.1021/ie403271t
16. Siepmann, J., & Siepmann, F. (2008). Mathematical modeling of drug delivery. *International Journal of Pharmaceutics*, *364*(2), 328–343. https://doi.org/10.1016/j.ijpharm.2008.09.004
17. Sun, W., Sun, C., Lin, H., Zhao, H., Wang, J., Ma, H., … Dai, J. (2009). The effect of collagen-binding NGF-β on the promotion of sciatic nerve regeneration in a rat sciatic nerve crush injury model. *Biomaterials*, *30*(27), 4649–4656. https://doi.org/10.1016/j.biomaterials.2009.05.037

18. Sun, Z., Zussman, E., Yarin, A. L., Wendorff, J. H., & Greiner, A. (2003). Compound Core–Shell Polymer Nanofibers by Co-Electrospinning. *Advanced Materials*, *15*(22), 1929–1932. https://doi.org/10.1002/adma.200305136

19. Tian, L., Prabhakaran, M. P., Hu, J., Chen, M., Besenbacher, F., & Ramakrishna, S. (2015). Coaxial electrospun poly(lactic acid)/silk fibroin nanofibers incorporated with nerve growth factor support the differentiation of neuronal stem cells. *RSC Advances*, *5*(62), 49838–49848. https://doi.org/10.1039/C5RA05773F

20. Tiwari, S. K., Tzezana, R., Zussman, E., & Venkatraman, S. S. (2010). Optimizing partition-controlled drug release from electrospun core–shell fibers. *International Journal of Pharmaceutics*, *392*(1–2), 209–217. https://doi.org/10.1016/j.ijpharm.2010.03.021

21. Wang, C., Yan, K.-W., Lin, Y.-D., & Hsieh, P. C. H. (2010). Biodegradable Core/Shell Fibers by Coaxial Electrospinning: Processing, Fiber Characterization, and Its Application in Sustained Drug Release. *Macromolecules*, *43*(15), 6389–6397. https://doi.org/10.1021/ma100423x

22. Wang, C.-Y., Liu, J.-J., Fan, C.-Y., Mo, X.-M., Ruan, H.-J., & Li, F.-F. (2012). The Effect of Aligned Core–Shell Nanofibres Delivering NGF on the Promotion of Sciatic Nerve Regeneration. *Journal of Biomaterials Science, Polymer Edition*, *23*(1–4), 167–184. https://doi.org/10.1163/092050610X545805

23. Xie, Z., Buschle-Diller, G., DeInnocentes, P., & Bird, R. C. (2011). Electrospun poly(D,L)-lactide nonwoven mats for biomedical application: Surface area shrinkage and surface entrapment. *Journal of Applied Polymer Science*, *122*(2), 1219–1225. https://doi.org/10.1002/app.34239

24. Yan, S., Xiaoqiang, L., Lianjiang, T., Chen, H., & Xiumei, M. (2009). Poly(l-lactide-co-ε-caprolactone) electrospun nanofibers for encapsulating and sustained releasing proteins. *Polymer*, *50*(17), 4212–4219. https://doi.org/10.1016/j.polymer.2009.06.058

25. Yang, F., Murugan, R., Wang, S., & Ramakrishna, S. (2005). Electrospinning of nano/micro scale poly(l-lactic acid) aligned fibers and their potential in neural tissue engineering. *Biomaterials*, *26*(15), 2603–2610. https://doi.org/10.1016/j.biomaterials.2004.06.051